



# City Research Online

## City St George's, University of London

**Citation:** Li, Q. & Bruecker, C. (2020). Sediment erosion in flexible canopies by vortex impact. *Journal of Fluids and Structures*, 97, 103058. doi: 10.1016/j.jfluidstructs.2020.103058

This is the accepted version of the paper.

This version of the publication may differ from the final published version. To cite this item please consult the publisher's version.

**Permanent repository link:** <https://openaccess.city.ac.uk/id/eprint/24255/>

**Link to published version:** <https://doi.org/10.1016/j.jfluidstructs.2020.103058>

**Copyright and Reuse:** Copyright and Moral Rights remain with the author(s) and/or copyright holders. Copies of full items can be used for personal research or study, educational, or not-for-profit purposes without prior permission or charge, unless otherwise indicated, provided that the authors, title and full bibliographic details are credited, a hyperlink and/or URL is given for the original metadata page and the content is not changed in any way. For full details of reuse please refer to [City Research Online policy](#).

# Sediment erosion in flexible canopies by vortex impact

Qianhui Li and Christoph H. Bruecker

School of Mathematics, Computer Science and Engineering, City, University of London, UK

## Abstract

A model experiment with a vortex impacting a flexible canopy filled with a thin homogeneous bed of particles is presented. Flexibility of the filaments increases the efficiency of resuspension by the amount it allows the effective canopy-height to reduce due to the reconfiguration of the flexible structures. Scaling of the results with the effective canopy height leads to a collapse of the observed resuspension in the history of several successive impacts. It is further shown that preferential pathways in the canopy play a large role in resuspension. When comparing a hexagonal arrangement to a random arrangement of the filaments at the same average porosity, one needs to double the amount of impacts to achieve the same average resuspension. Hence, it is concluded that the random path of the particles around the filaments is affected in a non-linear manner by the local resistance. Regions of locally sparse arrangements of the filaments cannot balance the trapping effect of particles within regions of dense arrangement in their travel history. Flexibility of the filaments again proves a better resuspension under such conditions.

Keywords: resuspension, vortex ring, flexible canopies

## 1. Introduction

Resuspension and erosion of particles by shearing flow widely exist in a series of natural phenomena such as sediment transport in rivers and dune formation in the desert. It also plays an important role in both industrial and environmental processes to control particle transport (Ouriemi et al. 2007). For example, it requires effective transportation of the particulate matter such as granular flow in food or pharmaceutical process via pipeline systems, whereas there is a requirement to prevent sediment resuspension in sewage sedimentation tanks and dust loss from soils which reduces soil fertility (Bethke and Dalziel 2012). Therefore, it is of great importance to understand the physical mechanism of sediment transport and redistribution to achieve effective control of it. Usually the sediment is nested within larger canopy layers such as the soil in crop fields, the sand layer in sea-grass, or canopies of larger scales as e.g. in forests. A recent review of turbulent flows over vegetation was given by Nepf (Nepf 2012) showing how fluid instabilities at the interface of the fluid-canopy layer modify the transfer of mass and moment within the canopy. A strong interaction is observed if the canopy is flexible and the elements in the canopy undergo considerable deformation, summarized in the review of wind over flexible canopies given by De Langre (De Langre 2008). However, as mentioned

37 in (Bethke and Dalziel 2012) the Reynolds number of the corresponding fluid flows is often high, which  
38 makes the understanding of particle transport underlying on the turbulent interaction of the fluid flow  
39 with the complex dynamics of the particles and the canopy structures difficult. Thus, a generally valid  
40 macroscopic model of particle transport in such configurations does not exist to date.

41 Recent numerical simulations of turbulent flow over canopies are able to include the elastic response  
42 of the structures. However, most of these studies are limited to low turbulent Reynolds numbers and  
43 for the linear-elastic regime. Bottaro (Bottaro 2019) was able to use multiscale homogenization for  
44 canopies consisting of periodic or quasi-periodic microstructures, avoiding the numerical resolution  
45 of small details such as the flow around individual elements of the canopy e.g. filaments. He  
46 considered the flow above solid surfaces with microscopic protrusions, with the wall roughness either  
47 rigid or linearly elastic and developed the underlying equations. This is relevant to the interaction of  
48 turbulent flows with filamentous walls, which are of growing interest for flow control along  
49 engineered aerodynamic / hydrodynamic surfaces (Bottaro 2019). The work also summarizes the  
50 recent developments in numerical simulations of canopy flows. The simulation most relevant to this  
51 study was done by Sundin and Bagheri (Sundin and Bagheri 2019), who simulated the interaction  
52 between hairy surfaces and turbulent flows in a turbulent channel flow configuration. Their work was  
53 inspired by the experimental observation of streak stabilization in turbulent boundary flows over  
54 arrays of flexible filaments (Brücker 2011). This two-way coupled interaction on different time-scales  
55 with the fluid flow and the mechanical system is difficult to achieve in numerical simulations as argued  
56 by Bottaro (Bottaro 2019). The pointwise approach used by Sundin & Bagheri (Sundin and Bagheri  
57 2019) may become difficult for dense coatings when the fluid simulation through the deforming  
58 filaments requires a more microscopic description. Furthermore, additional simulation of the  
59 transport of particles within the canopy may be out of reach at the current computational power of  
60 supercomputers. Therefore, further insight may be gained in laboratory experiments under controlled  
61 and repeatable conditions.

62 The experiments presented here address this need by studying the vortex-induced resuspension of  
63 particles within a canopy of slender flexible filaments, aiming to contribute to the growing interest for  
64 flow control along engineered aerodynamic / hydrodynamic surfaces built of such filamentous layers.  
65 In practical situations, the performance of such surfaces is often diminished by the accumulation of  
66 dust particles or other particulate matter in the layer. For effective two-way coupled interaction of  
67 the turbulent near-wall flow with the filaments, their typical length was chosen in the previous studies  
68 of order of the characteristic scale of the coherent vortex structures in turbulent boundary layers near  
69 the wall, the so called hairpin vortices (Brücker 2011, Sundin and Bagheri 2019). Instead of addressing  
70 the full range of turbulent scales, the present study follows the strategy of using a single vortex ring  
71 as a prototype of this elementary hairpin vortex structure, impacting with the canopy in a head-on  
72 collision. Such a prototypical model was first used by Sutherland (Sutherland 1967) for the study of  
73 resuspension in a sediment layer on a flat plate. We have set the Reynolds-number of the vortex ring  
74 to  $Re=800$ , which is comparable to that of a hairpin vortex near the wall (Bandyopadhyay and  
75 Balasubramanian 1995). The canopy height is chosen equivalent to the vortex-core radius and the

76 canopy properties (filament size, spacing, Cauchy-number) are leaned upon the recent numerical  
77 study of Sundin and Bagheri (Sundin and Bagheri 2019). They have studied numerically a turbulent  
78 channel flow at similar local ratio of the smallest vortex size to canopy height, and, as our canopy  
79 properties are similar, we might observe some similar features of the interaction. However, with the  
80 wall-normal impact of the vortex ring we are largely simplifying this turbulent interaction, mainly for  
81 practical, experimental reasons. The quasi-cyclic occurrence of coherent structures in turbulent flows  
82 and their penetration into the canopy is simulated herein with successive shoots of the vortex ring at  
83 the same location onto the canopy. This laboratory experiment with a laminar vortex-ring is therefore  
84 limited in relevance and conclusions to the specific conditions of the canopy, the vortex structure and  
85 the particles used herein rather holds as a benchmark test for numerical simulations under well-  
86 defined and repeatable boundary conditions. That those benchmark tests for engineered canopies are  
87 much needed and welcome to this community was recently highlighted by (Bottaro 2019) in his review  
88 article.

89 The present study might have some relevance in nature for Archerfish, as they are known for shooting  
90 jets underwater towards the sand floor to expose hidden prey or food (Dewenter et al. 2017). Therein,  
91 the fish use different angles and distances from the sand layer for generating a wash-out effect with  
92 formation of a sand cloud. The authors argue that the fish adapt their shots to different ground  
93 material when the fish explored for buried prey items; when food is buried in substrate that consists  
94 of large particles, the fish use a short pulse, but they use a longer one when the substrate is more fine-  
95 grained (Dewenter et al. 2017). The work differs from previous studies on vortex rings impacting with  
96 sand layers under water (Munro, Bethke, and Dalziel 2009, Bethke and Dalziel 2012) as the base herein  
97 is not a smooth flat wall but is formed as a canopy composed of slender filaments. The sediment layer  
98 consists of near-spherical sand particles with a mean diameter of 500  $\mu\text{m}$  and relative density of 1.36,  
99 which are initially homogeneous distributed in a horizontal layer within the forest of vertical posts of  
100 diameter 1mm and inter-spacing of 4mm (the canopy). A series of repeated vortex impacts is carried  
101 out while the deformation of the sand layer is recorded after each impact under otherwise constant  
102 parameters of vortex size, strength, velocity and travel path in a quiescent fluid. In one experiment,  
103 the posts of the canopy are rigid, in another experiment the posts are flexible and allowed to bend  
104 with the penetrating vortex. Furthermore, the arrangement of the posts is varied to study the effect  
105 of anisotropy of resistance and drag within the canopy. We compared a hexagonal grid of posts to a  
106 random grid at the same average porosity. The results are examined in terms of the effective  
107 resuspension, measured from the attenuation of light through the bed, while velocity field  
108 measurements complement the flow structure above the canopy layer during impact.

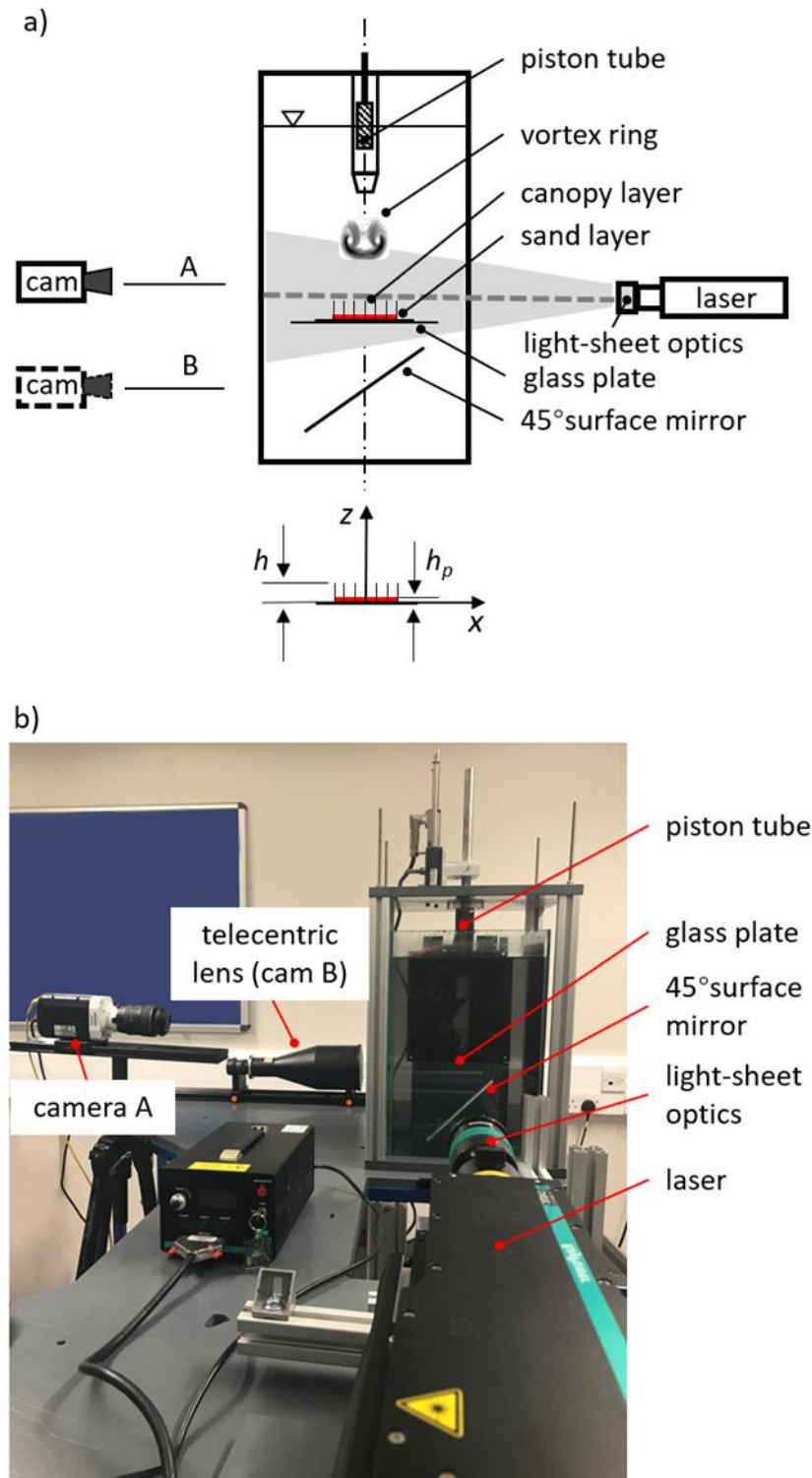
109

## 110 2. Experimental set-up and conditions

111 The experimental setup is shown in Fig. 1 following our previous study on the vortex interaction with  
112 a rough wall (Li and Bruecker 2018). A piston-cylinder nozzle (nozzle outlet diameter 30mm) is installed  
113 at the top of the liquid tank to generate the vortex ring with a radius of  $R = D/2 = 22 \text{ mm}$  at an initial

114 travelling speed of  $U_0 = 400$  mm/s. The radius of the vortex core is measured to  $R_c = 5$  mm. The  
115 calculated ring circulation follows  $\Gamma_0 = \int \omega_\theta dr dz$  and yields  $180$  cm<sup>2</sup>/s, resulting in a circulation-  
116 based Reynolds number  $Re_\Gamma = \Gamma_0/\nu = 800$ . The time is made non-dimensional in the form  $t^* =$   
117  $t\Gamma_0/R^2$  (it multiplies  $38$ /s with the physical time in seconds) and starts at zero when the roll-up process  
118 of the shear layer at the nozzle is finished. At  $20$  cm downstream from the nozzle exit, a transparent  
119 canopy layer with  $2$  mm thick disc-shaped base adhered on a glass plate is placed horizontally in the  
120 tank, below which a surface mirror is arranged  $45^\circ$  from the horizon and faces to the camera. As the  
121 vortex ring travels downstream, it impacts in a head-on collision with the canopy layer, which is  
122 formed by a forest of slender cylindrical posts. Within the canopy, a homogeneous layer of sand  
123 particles is placed. We observe the erosion of such particle layer during the impact of the vortex ring  
124 when the posts have different flexibility. The non-dimensional time of impact in the present study is  
125 defined at the moment when the free travelling vortex passes the origin of the coordinate system at  
126  $t_0^* = 15$ . An additional time scale  $T = t^* - t_0^*$  is defined to compare the different experiments after  
127 impact.

128



129

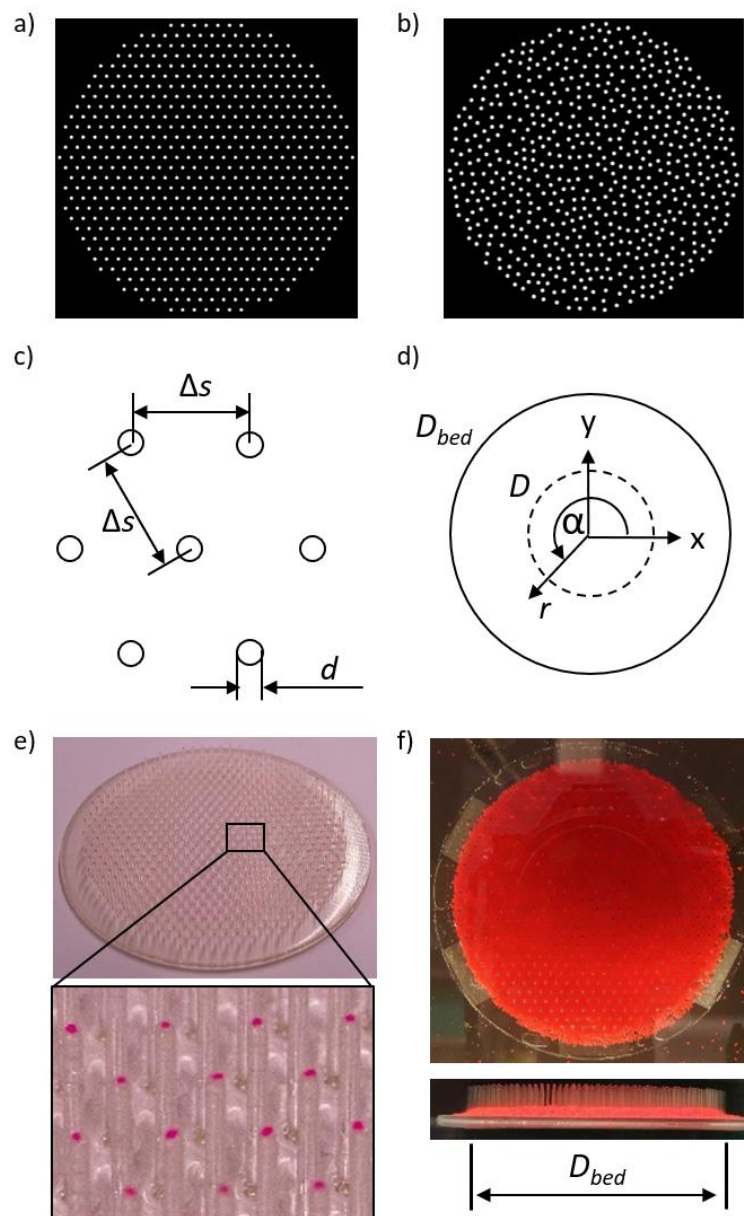
130 **Fig. 1.** Schematic of the experimental setup a) and picture of the actual flow rig b). The sketch in a)  
 131 shows the laser rotated into the paper plane. Camera configuration A is used with a vertical light-  
 132 sheet to record the flow field in the vertical  $x$ - $z$  plane; configuration B is used to record the flow field  
 133 in the radial  $x$ - $y$  plane above the canopy layer. Similarly, camera configuration A measures the  
 134 displacement of the flexible canopy filaments in the vertical  $x$ - $z$  plane while configuration B is used to  
 135 record the displacement of flexible canopies' tips in the radial  $x$ - $y$  plane. Finally, for sand layer erosion  
 136 measurements, the camera configuration B measures the intensity distribution of the light coming

137 from the top and travelling through the bed within the transparent canopy and base (glass plate),  
138 viewed by the camera through a 45° surface mirror. The coordinate origin is at the centre of the axis  
139 of the vortex ring on the surface of the glass plate.

140

141 Two canopy layers with the same dimension and structure but different flexibility are comparatively  
142 investigated. One type is composed of rigid filaments (rigid cylindrical posts of diameter  $d=1\text{mm}$  and  
143 height  $h=10\text{mm}$ ) and the other is composed of flexible filaments of the same cylindrical shape. As  
144 mentioned in the introduction, the height of the canopy layer is chosen equal to the characteristic size  
145 of the vortex core ( $2R_c = 10\text{ mm}$ ). The canopy layer with flexible filaments is cast from transparent  
146 silicone (Poly-Di-methyl-Siloxane PDMS, Wacker Silicones) (Young's modulus  $E \approx 1.24\text{ MPa}$ ), poured  
147 into a rigid mold which is perforated by laser drilling, see the method described in (Schmitz, Brücker,  
148 and Jacobs 2005). After curing, the cast with the filament is peeled off. The rigid one is made by 3D  
149 printing with transparent resin. The working liquid is a water- glycerol mixture (70/30 % by mass,  
150 density  $\rho = 1.18\text{ g/cm}^3$ , kinematic viscosity  $\nu = 22.5 \times 10^{-6}\text{ m}^2/\text{s}$ ) which matches the refractive  
151 index of the silicone material ( $n=1.4$ ). Fig. 2 shows the dimension and structure of the canopy layer  
152 and the particle layer. The slender posts are distributed in a regular grid  $(x_i, y_i)$  with a hexagonal pattern  
153 or alternatively in a random pattern, forming a porous canopy layer with an open interface at the top  
154 and closed interface at the wall. The average porosity of this layer is calculated by the ratio of void  
155 volume to total volume, yielding  $\epsilon=0.94$ . With the given conditions, our filamentous canopy structure  
156 is of similar structure as the filamentous wall used in the numerical study of Sundin and Bagheri  
157 (Sundin and Bagheri 2019) (in theirs  $h/d=5$ ,  $s/d=2$  and 4, in our study  $h/d=10$ ,  $s/d=4$ ). Furthermore,  
158 with the given material parameter of the silicone we reach the same filament Cauchy number of  $Q^*$   
159  $\sim 1$ , see below. Finally, the canopy height in their turbulent flow simulations is chosen such that it  
160 compares to the scales of the smallest coherent vortex structures (hairpin vortices) near the wall.  
161 Therefore, our study with the vortex ring is at a similar ratio of canopy height to characteristic vortex  
162 size, which let us assume stronger interaction with the bed similar as observed in their study.

163 Sand particles ( $\rho_p = 1.602\text{ g/cm}^3$  (dry)) with the average size of  $d_p = 500\text{ }\mu\text{m}$  are uniformly  
164 distributed within the canopy layer in a loosely-packed arrangement. Great care was taken to achieve  
165 a flat horizontal layer of the sediment with constant thickness prior to the impact experiments.



166

167 **Fig. 2.** Dimension and structure of the canopy layer. a) Slender filaments arranged in a hexagonal  
 168 lattice and b) in randomly distribution, with the same number density. c) Filaments with constant  
 169 diameter  $d = 1$  mm are spaced in the hexagonal grid as shown with  $\Delta s = 4$  mm. d) Coordinate systems  
 170 in the bed with diameter  $D_{bed} = 100$  mm, for comparison the torus of the vortex ring with diameter  
 171  $D = 44$  mm is indicated as a dashed circle. e) Picture of the canopy layer with filaments (initial height  
 172  $h = 10$  mm) protruding out. The tips of the canopy layer are fluorescent-labeled by fluorescent dye. f)  
 173 Bottom and side view of the sand layer uniformly distributed within the canopy.

174

175 Following the discussion of flexible wall-mounted filaments in flow (Brücker, Bauer, and Chaves 2007),  
 176 (Sundin and Bagheri 2019), the mechanical system of the filament can be described in first  
 177 approximation as a clamped cantilever beam and is described by the Euler-Bernoulli equation

$$EI \frac{\partial^4 q}{\partial z^4} + (\rho_s A + \chi) \frac{\partial^2 q}{\partial t^2} = f_{body} \quad (\text{eq. 1})$$

178 Here,  $q(t)$  is the filament displacement in the horizontal plane in direction of the horizontal flow vector  
 179 at the filament location (later in the article, the displacement  $Q$  at the tip of the filament is measured  
 180 as a vector in the horizontal plane at the surface of the canopy). The first term represents the force  
 181 due to the elastic bending of the filament, whereas the second describes the inertial force of the  
 182 acceleration and the third is the fluid-induced body force per unit length. By choosing proper reference  
 183 values, the system leads to two non-dimensional numbers, namely, the reduced velocity  $T^*$  and the  
 184 Cauchy number  $Q^*$  (Sundin and Bagheri 2019) . The first is

$$T^* = \frac{T_s}{T_f} = \frac{1}{T_f} \left( h^2 \sqrt{\frac{\rho_s A + \chi}{EI}} \right) \quad (\text{eq. 2})$$

185 where  $\rho_s$  is the density,  $A$  the cross-sectional area,  $E$  the Young's modulus and  $I$  the area moment of  
 186 inertia of a filament. The constant  $\chi$  represents the added mass. The numerator  $T_s$  is proportional to  
 187 the period of natural free vibrations of a filament in the fluid environment, which we measured as 120  
 188 ms in the working liquid. The characteristic time of the fluid fluctuations  $T_f$  is herein the inverse of the  
 189 velocity of the vortex ring divided by the diameter of the vortex ring, which calculates to 110ms. Thus,  
 190 the filaments adapt to approximately the same time-scale as the flow changes. The second number  
 191 represents a Cauchy number, which describes the static deformation under load:

$$Q^* = \frac{Q}{d/2} = \frac{\langle F \rangle h^3}{EI \cdot d/2} \quad (\text{eq. 3})$$

192 where  $\langle F \rangle$  is the acting integral force. The typical average bending  $Q$  of the filaments during the impact  
 193 is about one-times the filament diameter  $d$ , therefore both  $T^*$  and  $Q^*$  are of the order of 1, indicating  
 194 a strong fluid–structure interaction in the canopy. Note, that the average is taken over impact time  
 195 and over the area of the vortex ring impact zone. While the average is of the order of one-times the  
 196 filament diameter, peak values of the deflection for some of the filaments can reach locally around 4-  
 197 5-times the filament diameter, sometimes more than the filament inter-spacing.

198 The sediment resuspension is commonly described in terms of the Shields parameter

$$\theta = \tau / (\rho_p - \rho) g d_p \quad (\text{eq. 4})$$

199 where  $\tau$  is the bed shear stress (Munro, Bethke, and Dalziel 2009). Vertical lift-off of the particles  
 200 occurs when the lift force  $F_L = \pi \tau d_p^2$  exceeds the particle buoyancy. We could not measure herein  
 201 directly the bed shear-stress within the canopy, nevertheless the velocity field captured above the  
 202 canopy surface allowed us to track the vortex core during impact. Since the canopy height in our study  
 203 is of the same order as the size of the vortex core, we can expect a stronger correlation between the  
 204 bed wall-shear, the strength of the vortex and how far the vortex penetrates towards the bed when

205 impacting the canopy. We will look later in our results for possible correlations between regions of  
206 larger particle depletion, high radial velocity at the canopy surface (tangential to the tips of the forest  
207 of posts) and closest distance of the vortex core to the wall during the impact.

208 The measurements contain three parts as follows: firstly, the method of Time-Resolved Particle Image  
209 Velocimetry (TR-PIV) is used to obtain the flow field above the canopy. Secondly, the bending of the  
210 flexible filaments in the canopy is measured during the impact of the vortex ring by tracking their tips.  
211 Finally, the deformation of the suspension is measured by a light attenuation method, similar as  
212 described in (Bethke and Dalziel 2012). In the following, the methods are explained in more detail.

213

## 214 2.1 Velocity field measurements

215 The transparent flow chamber offers full optical access to different planes from the side and the  
216 bottom of the tank. A time-resolved PIV imaging system is used, comprised of a high-speed camera  
217 (Phantom Miro 310/311, Ametek) with CMOS sensor of 1280×800 pixels recording at 2000 frames per  
218 second, equipped with a lens (Tokima Macro  $f=100$  mm, F 2.8). The imaging magnification factor is  
219  $M=0.15$ . A continuous wave Argon-Ion laser (Raypower 5000, 5 W power at  $\lambda=532$  nm, Dantec  
220 Dynamics) holds as an illumination source. The output laser beam is about 1.5 mm in diameter and is  
221 further expanded to a sheet. For the experiments, the laser sheet is arranged in two variants: the flow  
222 field in the vertical x-z plane is recorded with the camera configuration A as shown in Fig. 1, looking  
223 from the side onto the flow in the vertical plane. For configuration B, the light-sheet is oriented in a  
224 horizontal x-y plane at a fixed height 1mm above the canopy in the fluid. Now, the camera looks from  
225 the side through a 45° mirror from the bottom of the tank in vertical upward direction through the  
226 transparent canopy onto the flow in the horizontal cross-section. As the sand particles now obstruct  
227 the optical access to the horizontal light-sheet plane above the canopy, we took these flow  
228 measurements in configuration B without any sand particle. We assume that the presence of the  
229 loosely-packed thin sand-layer at the floor of the canopy (max 3mm thickness) is of second-order  
230 influence onto the flow field of the approaching vortex-ring above the 10mm high canopy. This is  
231 because the dense forest of the 10mm high posts oppose the flow much stronger than the movable  
232 particles close to the floor. Comparative flow measurements above the canopy in the vertical plane  
233 (configuration A) without and with a 3mm thick loosely-packed sand layer at the canopy floor showed  
234 no discernible differences under the given flow conditions. Neutrally buoyant particles with a nominal  
235 diameter of 30  $\mu\text{m}$  are chosen as flow tracer. The data post-processing contains image pre-processing,  
236 2D cross-correlation of successive images to calculate the vectors following an iterative grid  
237 refinement method. For the flow field data, the final interrogation window has a size of 32×32 pixels  
238 and processing is done on a grid with 50% overlap ratio. The resulting vector grid is then used to  
239 calculate the out-of-plane component of the vorticity vector. For the case of the radial measurement  
240 plane, the equidistant Cartesian velocity grid is later interpolated onto a polar-type grid with constant  
241 spacing in radial and azimuthal direction with the velocity components  $v_r(r, \alpha)$  and  $v_\alpha(r, \alpha)$ .

242

## 243 2.2 Filament bending motion

244 The detection of the filaments' bending motion during the vortex impact is done by imaging the tip  
245 motion from the side and from below, see camera configuration A and B respectively. For the camera  
246 configuration B, the canopy is again not filled with the sand suspension with the same argument of  
247 optical access as given in section 2.1. Again, we assume that the presence of the thin sand-layer at the  
248 floor near the foot of the filament is only of second-order influence on the bending motion compared  
249 to the contribution to the tip bending due to the flow-induced load along the free end. Firstly, the  
250 particle layer at the floor is loosely-packed and free to relocate with the motion of the cantilever beam  
251 (filament) near the wall, therefore the mechanical behaviour of the cantilever beam (see eq. (1) and  
252 (3)) is basically not changed. Secondly, the bending of a one-sided clamped cantilever beam is  
253 dominated by the forces acting along the tip, while the forces near the foot contribute much less to  
254 the balance of moments, and therefore to the tip displacement. Comparative measurements of  
255 filament tip displacement from the side view (configuration A) without and with a 3mm thick loosely-  
256 packed sand layer at the canopy floor, finally, showed no discernible differences under the given flow  
257 conditions. To detect the tips, the filaments are fluorescent-labelled at the tip with a fluorescent dye  
258 containing Fluorescent Polymer Particles (PMMA-RhB-Frak-Particles, Dantec Dynamics). The peak in  
259 the emission spectrum of the fluorescent dye is at a wavelength of 584 nm, while maximum absorption  
260 is near the wavelength of the illuminating laser light. The camera lens is equipped with a long pass  
261 filter (transmission wavelength: 560 - 1650 nm, Edmund Optics Ltd), which blocks all light from the  
262 laser and reflections from the canopy, only transmitting the light of the fluorescent-labelled tips. Thus,  
263 the tips of the filaments appear as bright dots against a black background. See Fig. 4a and 4b for a  
264 comparison of images with and without the filter. In addition, the camera configuration B is equipped  
265 with a telecentric lens (Sill Optics) which offers parallel lines of sight when capturing the tips'  
266 displacement from a bottom view. This ensures that the image has constant magnification over the  
267 depth of the telecentric range. For the tip's displacement data, each image is cross-correlated with  
268 the first reference image, i.e. the resting condition before the impact of the vortex ring. The 2D cross-  
269 correlation processing is then done in small interrogation windows around the original positions of  
270 each spot  $(x_i, y_i)$  in the reference image. This provides the tip displacement vector field in each instant  
271 of the recorded series. To display as a contour plot, the tips' displacement vectors  $Q_r(x_i, y_i)$  are  
272 interpolated onto an equidistant Cartesian grid. Note that the tip's displacement is assumed to be  
273 proportional to the bed shear stress imposed by the radial fluid velocity component  $v_r(r, \alpha)$  above  
274 the layer surface. As argued by Munro et al. (Munro, Bethke, and Dalziel 2009), the bed shear stress  
275 is expected to be maximum directly below the vortex core.

276

## 277 2.3 Bed surface deformation

278 The measurements applied herein follow the light attenuation method documented earlier by Bethke  
279 and Dalziel (Bethke and Dalziel 2012). The bed of the particles is recorded with a camera from below,  
280 through the transparent glass wall. A light source is placed above the tank, illuminating the sand layer

281 from above. A mirrorless camera with 35mm full-frame CMOS image sensor (ILCE-7, Sony Ltd) is used  
 282 to capture the intensity field. The attenuation method assumes that the intensity of the diffusively  
 283 scattered light travelling through the thin bed is inverse proportional to the bed height  $h_p$ . This has  
 284 been proven by testing with three different thicknesses of homogeneous particle layers, which were  
 285 taken for calibration and validation of the method, see also previous applications of the method  
 286 reported in (Munro, Bethke, and Dalziel 2009). The first image before any impact of a vortex ring is  
 287 used as a reference when the particles are uniformly distributed and form a horizontal layer with  
 288 constant thickness in the quiescent flow tank. The corresponding intensity field is denoted as  
 289  $i_{n=0}(x, y)$ . The experimental procedure is as follows: from the initial condition with quiescent flow we  
 290 start with the first impact  $n = 1$ . The corresponding first snapshot image  $i_{n=1}(x, y)$  is captured when  
 291 all filaments are back to their original location (straight vertical) and any residual flow in the chamber  
 292 has ceased to zero. Successive impacts are then studied in the same way and snapshots  $i_n(x, y)$  are  
 293 taken one after the other. With each shoot, the near-surface particles in the region of maximum shear  
 294 stress directly below the ring core are transported, resulting in the formation of a circular mound, the  
 295 radius of which increases as the vortex is stretched, see also (Munro, Bethke, and Dalziel 2009).  
 296 Therefore, the intensity in the region of the mound decreases and the image gets darker there.  
 297 Meanwhile, at the region of highest bed wall-shear, the particle erosion leads to increase of the  
 298 intensity. We stop the experiments when we observe first signs (small empty patches) of local  
 299 complete particle depletion in the evolving erosion crater, i.e. the crater has reached the floor.

300 In the image processing, we blank the circular areas at the filament foot positions and use only the  
 301 regions between the straight filaments for data processing. The non-dimensional intensity field is  
 302 calculated for each shoot as  $I_n(x, y) = [i_0(x, y) - i_n(x, y)]/i_0(x, y)$  and transferred with the  
 303 calibration function into a surface deformation  $\Delta h_{p,n}(x, y)$  of the bed. The uncertainty of the given  
 304 values in  $\Delta h_p$  is  $\pm 0.1\text{mm}$ , which is obtained from the calibration procedure. We define herein  $\sigma_n$  as  
 305 an accumulated resuspension value, which is calculated as the standard deviation of  $\Delta h_{p,n}(x, y)$ ,  
 306 equivalent to the RMS roughness of the deformed surface. Therefore it takes into account not only  
 307 particle depletion but also re-deposition in the impact region, both contributing to the surface  
 308 deformation.

309 For comparison, we take the flexible case as a reference.  $N_{flex}$  is the number of impacts until the eroded  
 310 crater reaches the floor. The measured resuspension value at this stage is used as a reference for the  
 311 rigid case and we look in the data how many impacts  $N_{rigid}$  were needed to reach the same level of  
 312 resuspension. These data are then collected in a table to illustrate the difference of the configurations  
 313 tested. Quantitative data are shown as normalized values, plotting the normalized resuspension  
 314  $\bar{\sigma}_n = \sigma_n/\sigma_{N_{flex}}$  over the normalized impact number defined as  $\bar{n} = n/N_{flex}$ .

315

316

317

318

## 319 2.4 Bed and Canopy configurations

320 A series of configurations with different particle bed height  $h_p$ , filament stiffness and arrangement are  
 321 investigated as shown in Table 1. A pair of cases with the same bed height but different filament  
 322 flexibility such as Case RH20 and Case FH20 works as a comparison pair. The table provides also the  
 323 total impact times  $N$  until first empty patches occur in the sediment at the valley of the crater. The  
 324 results show that  $N$  is always smaller for the flexible filaments configuration compared to the rigid  
 325 ones.

326

327 **Table 1.** Geometric and dynamic properties of the configurations that are investigated.

Case	Filament traits	Filament arrangement	$h_p$ (mm)	$h$ (mm)	$h_p/h$	$N$
RH10	Rigid	Hexagonal	1	10	0.1	10
FH10	Flexible	Hexagonal	1	10	0.1	8
RH20	Rigid	Hexagonal	2	10	0.2	32
FH20	Flexible	Hexagonal	2	10	0.2	24
RH30	Rigid	Hexagonal	3	10	0.3	62
FH30	Flexible	Hexagonal	3	10	0.3	44
RR30	Rigid	Random	3	10	0.3	104
FR30	Flexible	Random	3	10	0.3	80
SH	Rigid	Hexagonal	3	3	1	17
FW	Flat wall	-	3	-	-	4

328

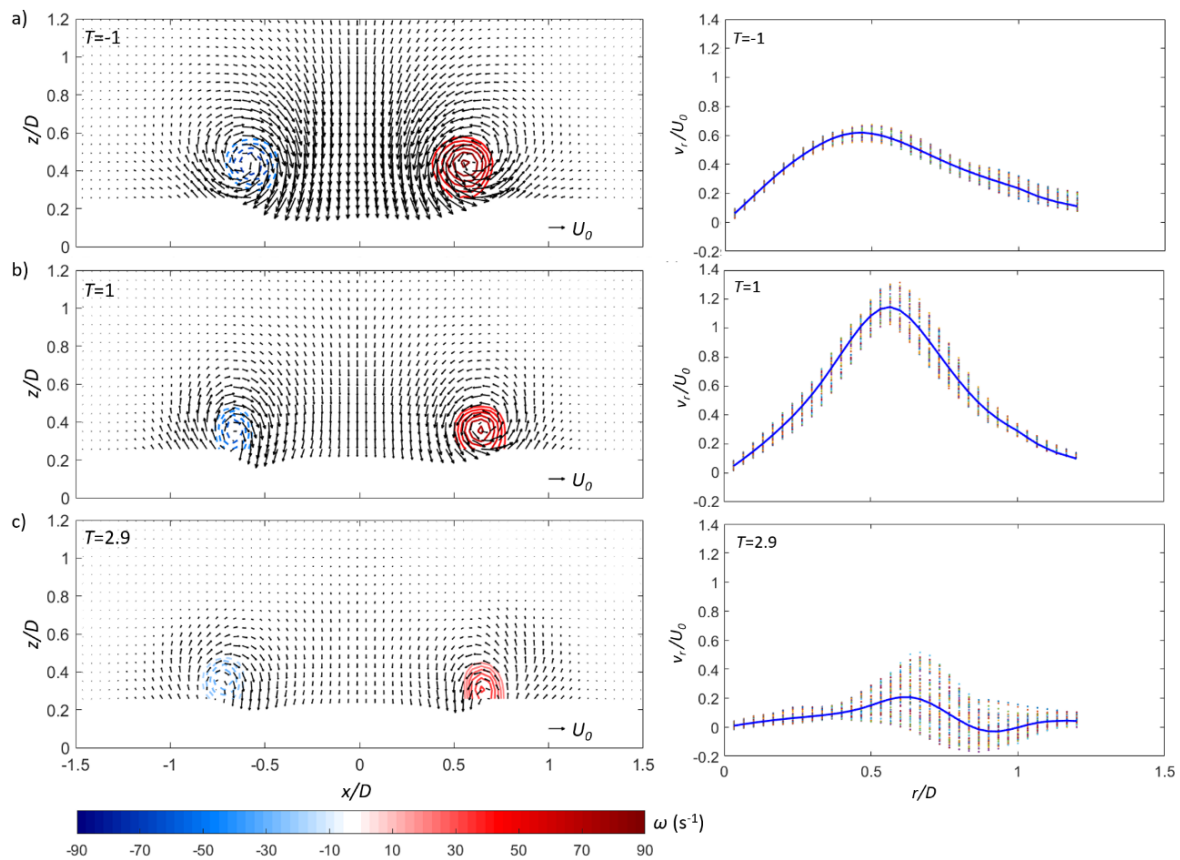
329

330 **3. Results**

331 The flow evolution above the canopy is shown in Fig. 3 for the flexible filaments configuration. The  
 332 left column presents the vertical flow field while the right column displays the corresponding radial  
 333 flow evolution at the horizontal interface between the main flow and canopy layer. The initial phase  
 334 of approach and first contact with the canopy layer occurs at  $T=-1$ . Then the primary vortex ring  
 335 expands to a radius of  $\sim 0.6D$  at  $T=1$  when impacting and thereafter slightly expands further over  $1.9T$   
 336 time period. As the vortex approaches the canopy it generates a strong radial velocity parallel to the  
 337 canopy surface below the core, induced by the tangential velocity at the edge of the vortex core  
 338  $\Gamma_0/(\pi R_c)$ . The location of peak radial velocity occurs directly below the vortex core and shifts from  
 339  $r/D \sim 0.45$  at the first contact to  $r/D \sim 0.6$  when impacting, and further to  $r/D \sim 0.65$  at  $T=2.9$ . The  
 340 tangential velocity as well as the core vorticity decrease during the penetration into the canopy layer,  
 341 indicating the effect of dissipation imposed by the posts within the porous layer.

342

343



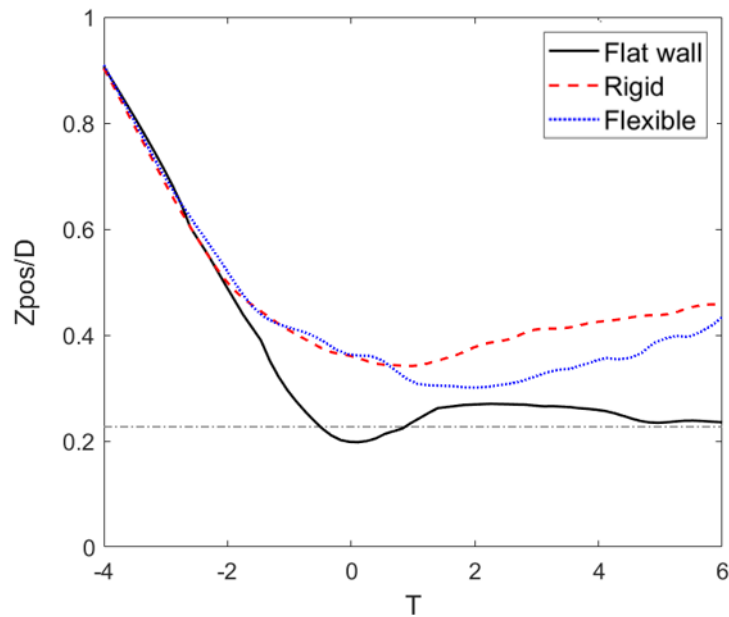
344

345 **Fig. 3.** Velocity field in the vertical plane overlaid with vorticity contours are shown in the left column.  
 346 The right column displays the mean of the radial velocity (averaged over the circumference) plotted  
 347 over the radius in the horizontal plane 1mm above the canopy (blue solid line). The colored dots  
 348 illustrate the variation of  $v_r(r, \alpha)$  over the circumference.

349

350 Fig. 4 shows the track of the centre of the primary vortex core over time for the different canopy  
 351 configurations (flat wall, 10mm rigid canopy, 10mm flexible canopy), plotted as the wall-normal  
 352 distance over time. This is derived from the cross-sectional vorticity field in each time-step by  
 353 searching for the peak location in the vorticity field, see Fig. 3. The data at the maximum are fitted  
 354 with a 3-point 1-D Gaussian fit in both x- and z-direction to achieve higher precision. The major outcome  
 355 for the canopy with flexible filaments is that the vortex core during impact gets closer towards the  
 356 wall than for the rigid one before it rebounds again.

357



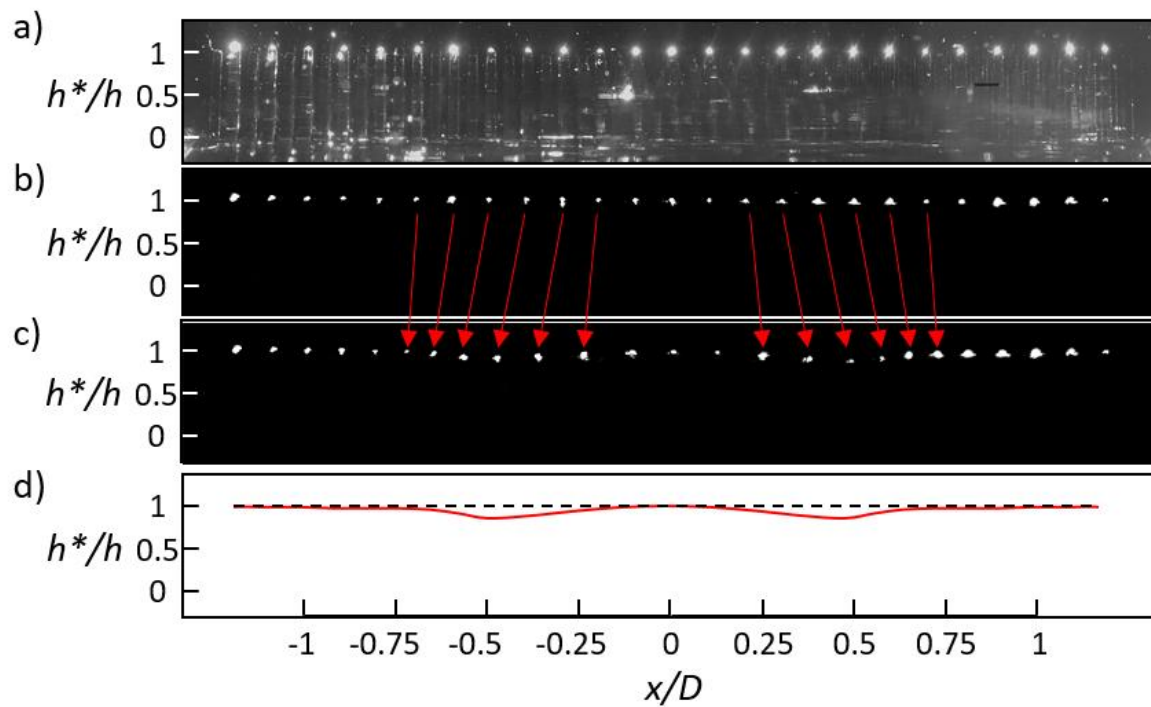
358

359 **Fig. 4.** History of the wall-normal distance of the vortex core position during the impact of the vortex  
 360 ring in the vertical centre plane ( $x$ - $z$  plane). The grey dash-dot line denoted the location of the surface  
 361 of the canopy relative to the flat wall.

362

363 Fig. 5 illustrates exemplarily the deflection of the flexible filaments along one row through the centre  
 364 for  $T=1$ . As seen by the strong deflection of the tips, the surface can quickly comply with the vortex  
 365 impact, opening up its interface. Thus it allows the core to penetrate further towards the bed as in the  
 366 case of the rigid canopy, see Fig. 4. For mechanical reasons, strong lateral bending of the filaments  
 367 also leads to a considerable lowering of the tip in vertical direction, effectively seen by the indentation  
 368 of the interface, most pregnant at time  $T=1$  in regions of maximum lateral bending at about  $x/D \sim 0.5$ -  
 369  $0.6$ . Comparing the flow field at the same time  $T=1$ , this region is at the radial position where the  
 370 vortex core penetrates into the canopy and where the maximum radial velocity is observed at the  
 371 interface, see Fig. 3. The effective height of the canopy is there reduced down to  $h^* = 85\% h$ . As the  
 372 size of the vortex core is similar to the canopy height in our study, we expect an increase of the bed  
 373 wall-shear the deeper the vortex can indent the interface and penetrate towards the bed. We will look  
 374 later in our results for a possible correlation between regions of larger particle depletion and filament  
 375 bending (interface indentation).

376

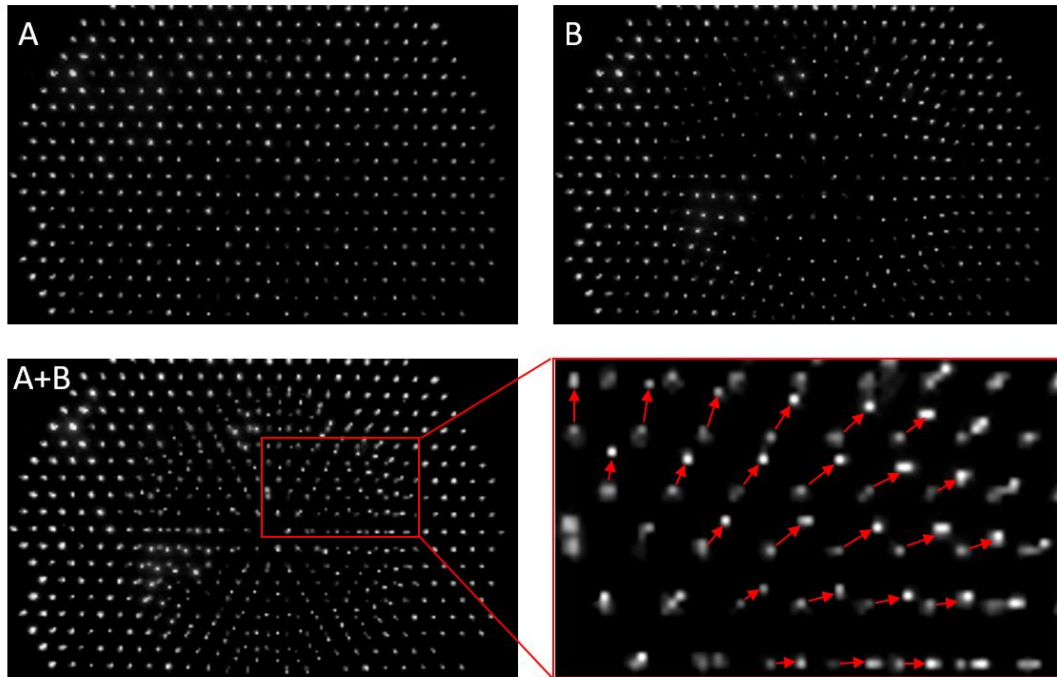


377

378 **Fig. 5.** a) Image of a row of flexible filaments in the vertical  $x$ - $z$  plane before vortex ring impact. When  
 379 putting the long pass filter on, the reflections along the filaments are filtered out and only the tips  
 380 appear as the bright spots in b). Impacting of the vortex ring on the canopy layer cause the bending of  
 381 the flexible canopy, the tips' displacement of which are shown in c). d) The plot of the effective height  
 382  $h^*$  profile of the flexible canopy interface (denoted by the red solid line), compared with reference  
 383 height  $h$  before the impact (denoted by the black dash line).

384

385 Fig. 6 displays the bottom view of the tip locations before ( $T=-\infty$ ) and after the impact at  $T=1$  by Image  
 386 A and Image B separately. By overlaying Image B on Image A, we obtain a combination image showing  
 387 the tip displacement vectors  $Q_r(x_i, y_i)$  in the hexagonal pattern. Also, from the zoom-in view, one can  
 388 see that maximum tip displacement can reach the distance of the inter-spacing between neighbouring  
 389 filaments.

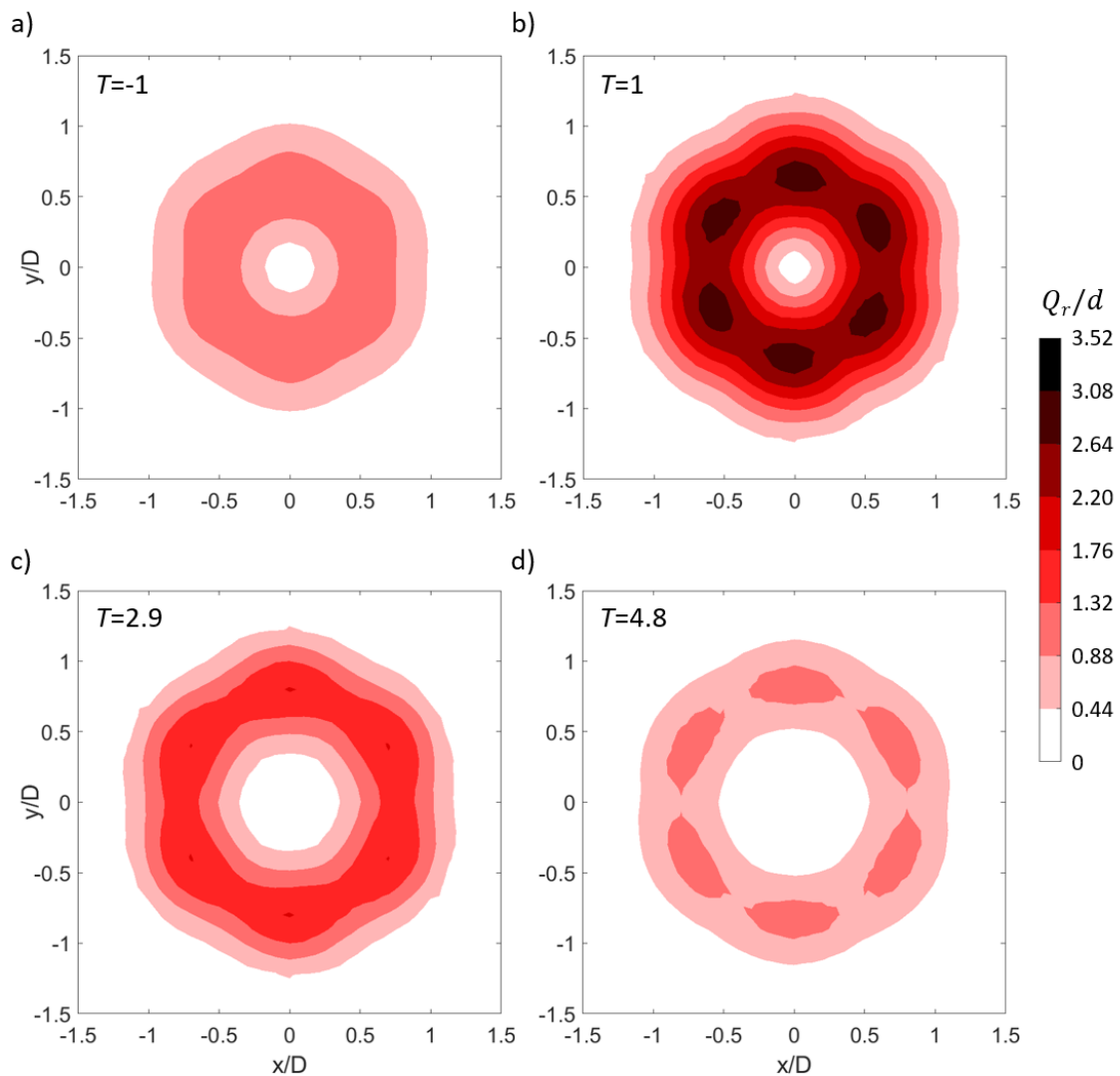


390

391 **Fig. 6.** Images of filament tips before the impact of the vortex ring (image A,  $T = -\infty$ ) and at the impact  
392 (image B,  $T=1$ ). The combination (image A+B) of image A and B shows the displacement of the tips,  
393 with denoted by red arrows in a zoom-in view.

394

395 Since the vectors are pointing approximately radially outwards from the centre of the canopy (the axis  
396 of the impacting vortex ring), the dominant component of  $Q_r(x,y,T)$  is the radial component. Further  
397 information is obtained from contour plots of  $Q_r(x,y,T)$  over several time steps, see Fig. 7.



398

399 **Fig. 7.** Evolution of the contours of the tip displacement for flexible filaments configuration at a)  $T=-1$ ,  
 400 b)  $T=1$ , c)  $T=2.9$  and d)  $T=4.8$ . The tip's displacement  $Q_r(x,y,T)$  is normalised by the filament diameter  
 401  $d$ .

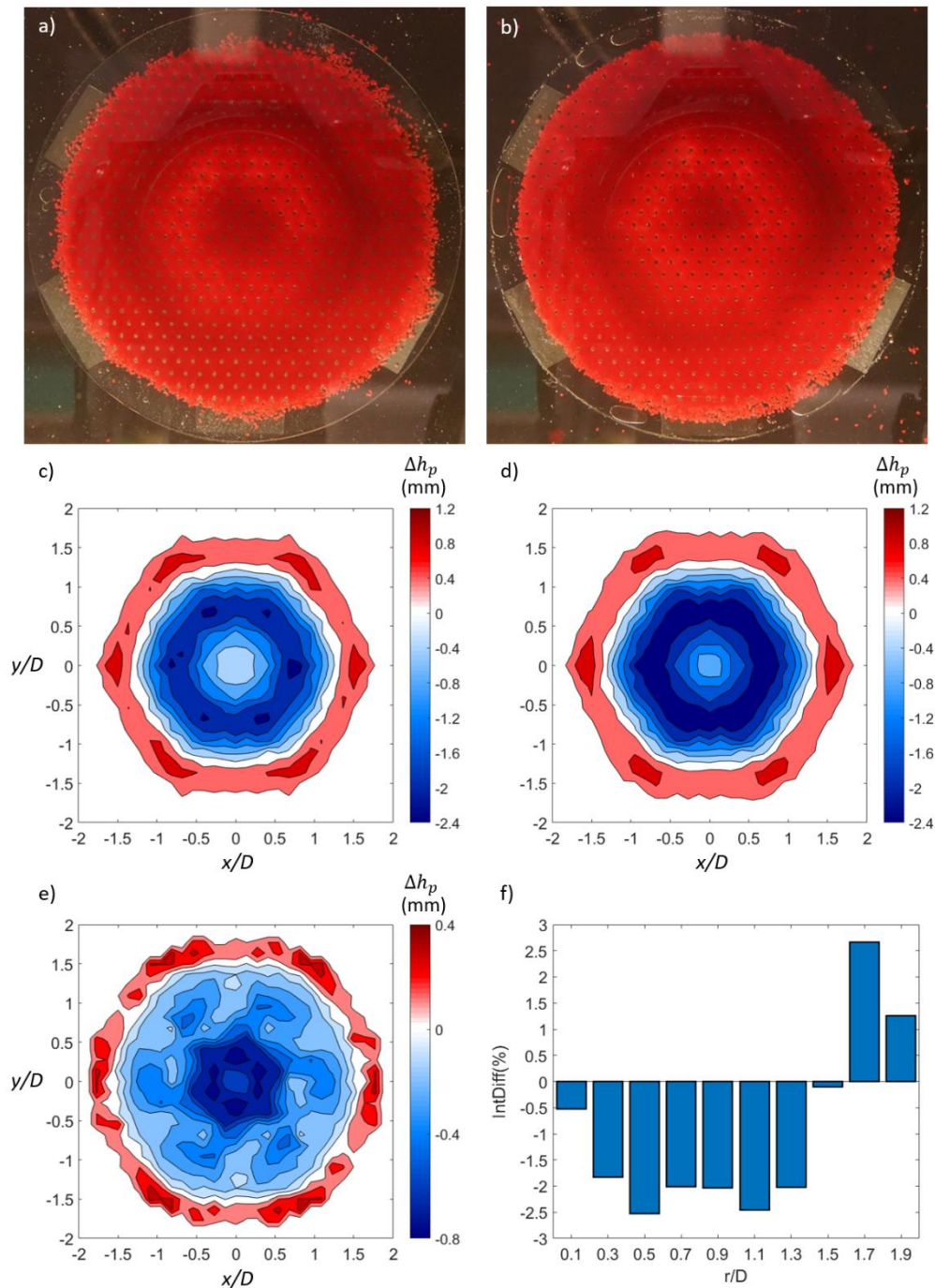
402

403 The contours of the displacement field are not perfect axisymmetric but show a footprint of the  
 404 hexagonal structure of the canopy. Previous studies in our lab haven proven that the vortex ring  
 405 deforms into a hexagonal pattern after impact due to a lock-in effect of the azimuthal instability with  
 406 the hexagonal grid (Li and Bruecker 2018). Interestingly, the peak values of  $Q_r$  occur not along the  
 407 preferential pathways along  $\alpha = 0^\circ + j * 60^\circ$  ( $j = 1,2,3 \dots$ ) but in between at angles of  $\alpha = 30^\circ +$   
 408  $j * 60^\circ$  ( $j = 1,2,3 \dots$ ). The average radius of maximum radial tip displacement is at about  $0.5-0.6 D$  at  
 409 the beginning of impact and it expands to  $0.8D$  at the late phase when peak values of bending decrease  
 410 down to the order of  $1d$ .

411

412 When repeating the experiments with the sand-layer inside the canopy we see the evolution of a  
 413 similar hexagonal pattern of the deformed sediment. A comparison of the typical distribution after  $n$   
 414 = 44 shoots for the rigid and the flexible canopy is illustrated in Fig. 8.

415



416

417 **Fig. 8.** Images showing the crater pattern eroded by the impact of vortex ring after  $n=44$  times of  
 418 impact for case RH30 a) and FH30 b). Corresponding contours of the bed surface deformation in mm  
 419 are shown in c) and d). e) Contour plot of difference in local bed surface height between FH30 and  
 420 RH30; f) bar chart of the difference in percentage of the total bed volume within the impact region ( $r$

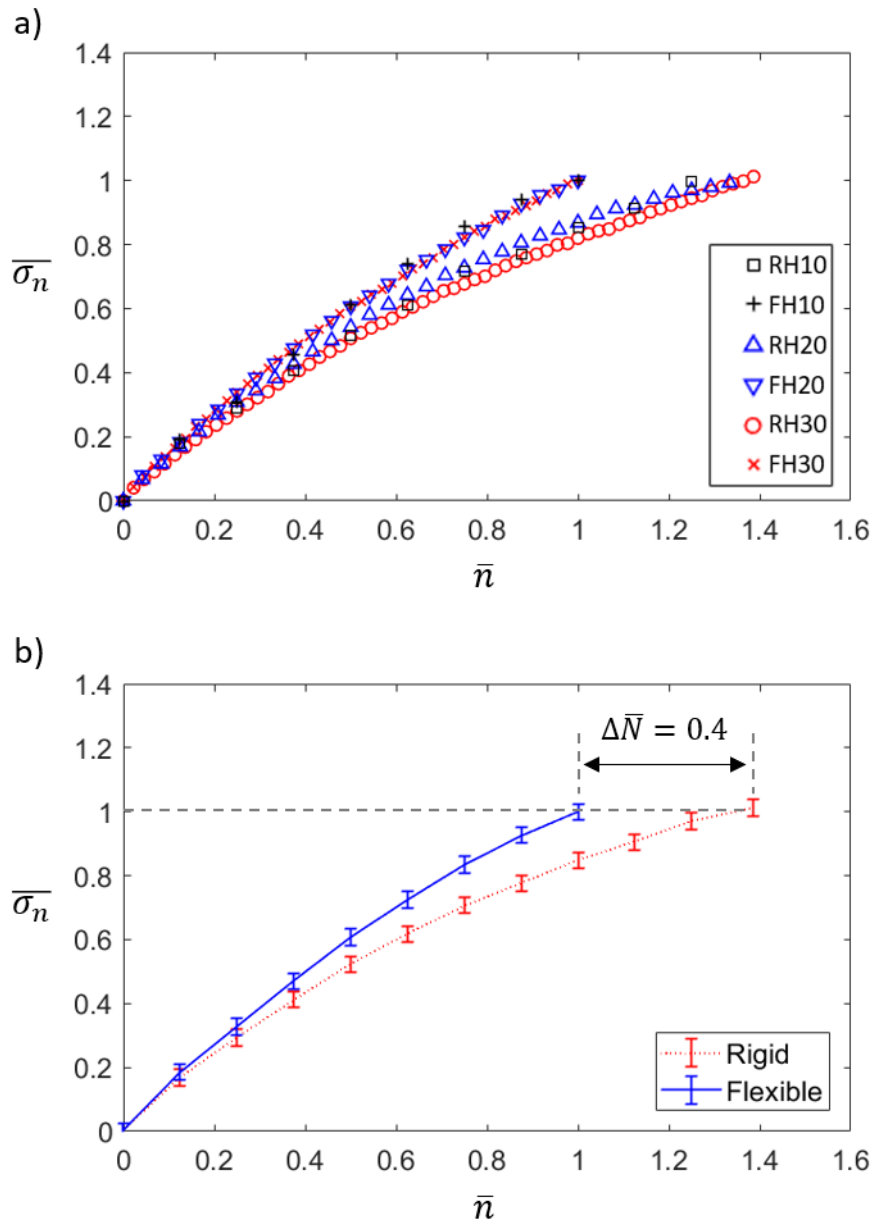
421  $\leq 1.3D$ ). The values are obtained by integrating the contours in e) over different circular ring areas of  
422  $\Delta r=0.2D$  ( $\sim 2\Delta s$ ).

423

424 Similar as observed in (Munro, Bethke, and Dalziel 2009) for a single shoot experiment on a flat wall,  
425 we observe after several shoots the slow formation of a crater. Maximum particle depletion occurs at  
426 a radius of  $r/D\sim 0.6$  (ring of dark blue), just in the region below the vortex core where the radial  
427 velocity at the interface of the canopy is maximum. On the other hand, particles are accumulated in a  
428 ring at a larger diameter  $r/D\sim 1.5$ , building the crest of the crater. Furthermore, we also see a small  
429 mound of uneroded particles remaining at the crater centre below the axial stagnation point of the  
430 vortex ring. These results demonstrate that the ring-like region of maximum particle depletion (at  
431  $r/D\sim 0.6$ ) agrees with the location of peak radial velocity at the surface of the canopy during the  
432 impact in Fig. 3b, therefore regions of elevated levels of bed wall-shear are seemingly correlated with  
433 regions of high radial velocity at the canopy surface.

434 As a striking feature of our experiment, the crater is not perfect circular but shows a hexagonal pattern  
435 of the crest, orientated in the same way as the hexagonal pattern of the canopy (see (Li and Bruecker  
436 2018)). The local maxima along the crest of the crater are aligned with the orientation of the  
437 preferential pathways in the canopy. Comparing the results for the flexible case FH30 with the rigid  
438 one RH30 shows that the diameter of the hexagonal crest is a bit larger, in addition the magnitude of  
439 particle depletion in the crater is more pronounced. The difference between the bed surface levels of  
440 FH30 and RH30 is included as a subplot in Fig. 8e. For further clarification, we show in Fig. 8f the  
441 percentage of bed volume which the flexible case is able to further resuspend compared to the rigid  
442 one. The values, integrated along different circular ring diameters, show that more particles have  
443 eroded from the crater valley region and relocated at the outer crater crest than for the rigid case.  
444 What can be seen is a surplus of about 13% of bed volume more removed from the crater, and 4%  
445 more added to the growth of the crest. This demonstrates that flexibility of the posts has promoted  
446 particle resuspension under otherwise identical initial and boundary conditions. Note, that surface  
447 levels at  $r > 1.9D$  are not captured in the image processing and particles may have left their original  
448 region completely, therefore the percentages in Fig. 8f in sum do not necessary cancel out to zero.  
449 Rather, it shows that there is also a surplus in net radial outflux of the bed volume at the canopy  
450 border for the flexible case, which is about 9% higher.

451



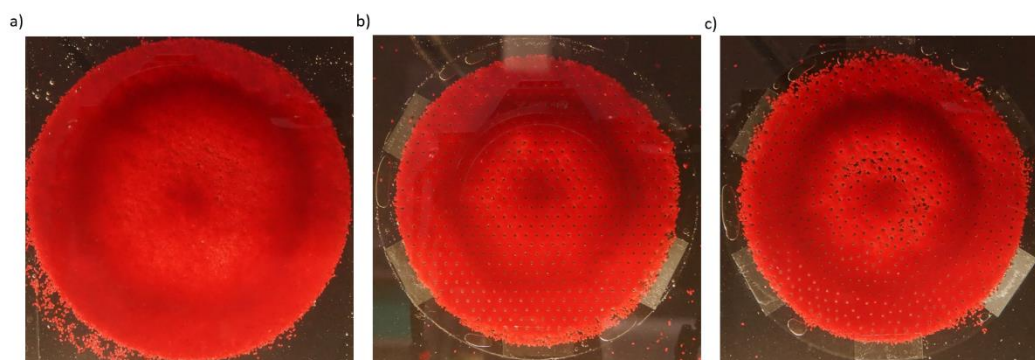
452

453 **Fig. 9. a)** Plots of the accumulated effective resuspension  $\overline{\sigma}_n$  over the amount of impacts of the vortex  
 454 ring for rigid canopy and flexible canopy for three sets of bed thicknesses. The details of configurations  
 455 are listed in Table 1. For each comparison pair, the effective resuspension is normalised by  $\sigma_{N_{flex}}$  of  
 456 the flexible filaments configuration.  $\bar{n}$  is the normalized number of impacts, defined as impact number  
 457  $n$  divided by the total number of impacts  $N_{flex}$  of the flexible filaments configuration. b) Plots of mean  
 458 normalized resuspension of rigid canopy and flexible canopy respectively with error bars.

459

460 We further plot the history of the accumulated resuspension  $\sigma_n$  over increasing number of shoots for  
 461 all experiments in a single diagram, see Fig. 9. When we initially did that, we saw that the profiles look  
 462 self-similar. Therefore, we show the profiles in a normalized form by plotting  $\overline{\sigma}_n = \sigma_n / \sigma_{N_{flex}}$  over the  
 463 impact number  $\bar{n} = n / N_{flex}$  (recall that the characteristic impact number  $N$  for the flexible canopy is

464 always less than that for the rigid canopy). Firstly, the normalization shows that the profiles for the  
 465 flexible cases collapse into approximately one single curve for all different bed thicknesses. The same  
 466 holds for the experiments with the rigid canopies, though the scatter is somewhat larger. Secondly,  
 467 plotting the average for the different bed thicknesses together with the error-bars illustrates that the  
 468 scatter is well within the range of the measurement uncertainty, therefore the observed behaviour  
 469 clearly demonstrates a physical reason for the different trends in both curves. They show for the same  
 470 values of  $\overline{\sigma}_n$  constantly an approximately 20% higher accumulated effective resuspension for the  
 471 flexible canopy. Alternatively, one can interpret the data along the horizontal axis. We observe for the  
 472 rigid canopy about 40% lower resuspension rate (accumulated resuspension per impacts), highlighted  
 473 by  $\Delta\bar{N} = 0.4$  at  $\overline{\sigma}_n = 1$  in Fig. 9b.



474

475 **Fig. 10.** Images showing the crater pattern eroded by the impact of the vortex ring in configuration of  
 476 particle layer thickness  $h_p = 0.3h$  for a) flat wall after  $N = 4$  impacts, b) FH30 after  $N = 44$  impacts and  
 477 c) FR30 after  $N = 80$  impacts.

478

479 Finally, a comparison of the intensity field for the random arrangement in Fig. 10 proves that the  
 480 hexagonal pattern of the crater in Fig. 8 is indeed a consequence of the underlying canopy structure.  
 481 With a random arrangement of the posts in the forest, the crater approaches a rather circular shape.  
 482 However, the necessary number of successive shoots to reach the same effective resuspension has  
 483 increased about a factor of two, see Tab. 1. Nevertheless, the flexible canopy again reaches this state  
 484 much earlier as seen from Tab. 1.

485

## 486 4 Discussion

487 Comparing the resuspension of particles in a canopy of the same geometry with rigid posts and flexible  
 488 posts of the same shape concludes that flexibility of the posts has improved resuspension. What can  
 489 be seen is a surplus of about 13% of bed volume more removed from the crater in the region  
 490  $0.5 \leq r/D \leq 1.1$ , which agrees with the region of considerable tip displacement of the filaments  
 491 radially outwards with values of  $Q \geq 1d$  during the impact of the vortex ring. At the inner part of this  
 492 region in  $0.5 \leq r/D \leq 0.8$  is where a) the strongest indentation of the canopy surface is observed, b)

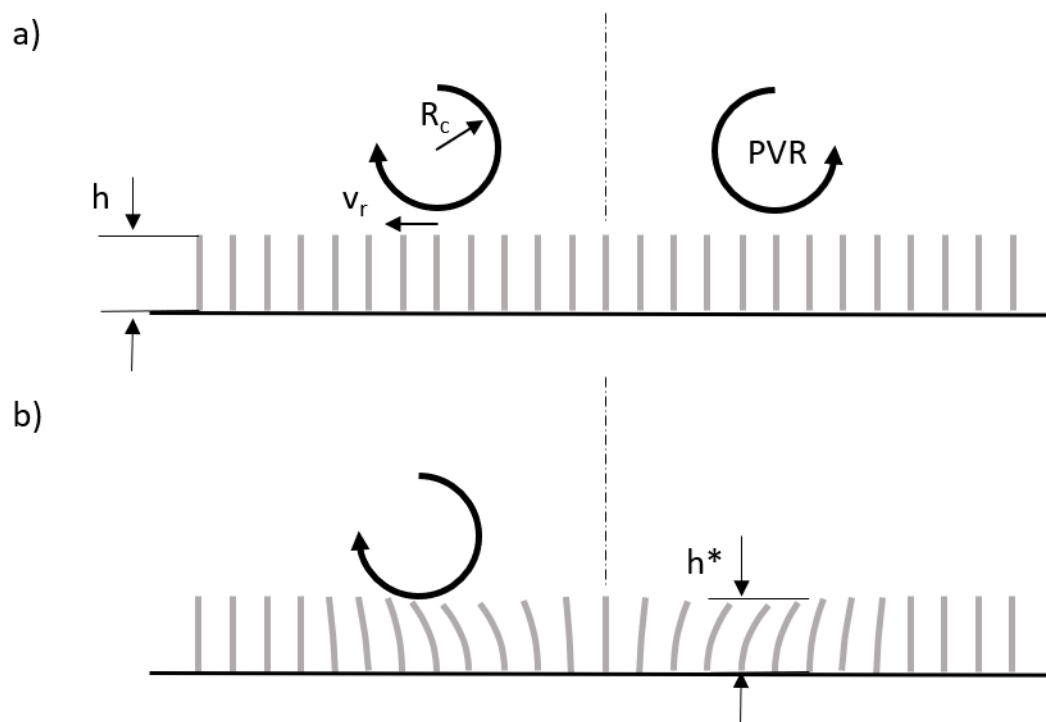
493 maximum radial velocities at the interface are observed and c) the vortex core penetrates closer  
 494 towards the bed. Under the given conditions of canopy height equal to the vortex-core size and the  
 495 given canopy properties (filament size, spacing, Cauchy-number), these results prove the strong  
 496 correlation between locations of peak bed shear-stress (maximum of particle depletion), peak radial  
 497 velocity at the interface to the canopy and peak indentation. Based on these results we propose a  
 498 conceptional model for the given situation, which assumes in first approximation that the bed wall-  
 499 shear is proportional to the strength  $\Gamma_0$  of the impacting vortex and inversely proportional to the  
 500 canopy height  $h^*$ , see Fig. 11 and eq. (5) with  $\nu$  as the kinematic viscosity of the fluid.

$$\tau \approx \nu \rho \frac{\Gamma_0 / (\pi R_c)}{h^*} \quad (\text{eq. 5})$$

501 The expression of the vortex strength in form of  $\Gamma_0 / (\pi R_c)$  describes the radial velocity at the  
 502 interface when the edge of the vortex core reaches the canopy, which was measured in our  
 503 experiments. In addition, the height  $h^*$  indicating the indentation of the penetrating vortex was  
 504 measured optically, too. Following the hypothesis given in eq. (5) one can compare the curves of  
 505 effective resuspension between the rigid canopy and the flexible canopy in Fig. 9 if one takes into  
 506 account the effect of the indentation of the canopy (the strength of the vortex is unchanged). Recall,  
 507 the effective height shows a typical value  $h^* = 85\%h$  at maximum canopy indentation, which is radially  
 508 moving over the course of impact from  $r/D \sim 0.5$  to  $r/D \sim 0.8$ . Therefore, following eq. (5) the wall-shear  
 509 stress acting on the bed at this location is about 17% higher than in the rigid case. When applying this  
 510 correction to the flexible case (reducing the  $\bar{\sigma}_n$  values about 17%), both curves of effective  
 511 resuspension in Fig. 9b can get to near overlap. The so achieved overlap supports the conceptional  
 512 model and the assumption in eq. (5), although the exact functional description therein is not known  
 513 yet. As in a porous medium the velocity exponentially reaches a Darcy flow (e.g. Brinkman layer), more  
 514 accurate estimation is only possible with direct measurements inside the canopy. However, it is  
 515 reasonable to argue in our case that the bending of the pillars increases locally the permeability of the  
 516 bed, allowing fluid to more easily penetrate, which in turn increases shear stress. Sundin and Bagheri  
 517 (Sundin and Bagheri 2019) concluded, that such surfaces with soft filaments in turbulent channel flow  
 518 increase the entrainment of free fluid into the bed and may be useful in application where mixing and  
 519 entrainment are beneficial. The present results confirm the enhanced mixing in the flexible canopy.

520

521



522

523 **Fig. 11.** Conceptual model of the impacting of the vortex ring on the compliant canopy layer: a) the  
 524 primary vortex ring (PVR) with the core radius  $R_c$  approaches the tips of the canopy layer. The vorticity  
 525 induces a strong radial outwards-direct velocity component  $v_r$  at the interface underneath the vortex  
 526 core, inducing locally strong filament bending. b) the indentation of the interface effectively reduces  
 527 the height of the canopy layer  $h^*$  and allows the vortex core to penetrate deeper towards the bed  
 528 floor.

529

530 The crater measurements herein show in general many similarities to the results obtained in single  
 531 shots of vortex rings on sand-layers on a smooth flat wall (Munro, Bethke, and Dalziel 2009). With the  
 532 underlying canopy structure, it requires much more shoots to achieve considerable resuspension due  
 533 to the resistance within the canopy layer, however the global pattern resembles those with a single  
 534 shoot in a plane wall. If the canopy has preferential pathways due to anisotropic arrangements of the  
 535 posts or other structural elements, the overall performance of resuspension improves and the crest  
 536 of the crater deforms accordingly. A proof is given by recovering a hexagonal structure of the crest of  
 537 the crater after several shoots when the underlying grid of posts has a hexagonal arrangement.  
 538 Interestingly, if a canopy of the same porosity is studied with a random arrangement of the posts, the  
 539 effective resuspension is largely reduced. This is probably because of the tortuosity of the particle  
 540 paths while moving through the forest of posts and the non-linear characteristics of bed resistance in  
 541 local unit-cells of posts with different mean porosity. It is assumed that particles remain much longer  
 542 trapped in regions of posts with high local density than they are free to move in sparser regions.

543

## 544 5. Conclusions

545

546 The following conclusions are based on the above described laboratory experiment under well defined  
547 and ideal conditions of the impact of an axisymmetric laminar vortex ring on the canopies. Most  
548 importantly, the height of the canopy here corresponds to the size of the vortex core. This is not  
549 directly transferable to the situation of turbulent flows over natural canopies, but it's being  
550 investigated here as a benchmark experiment to understand the interaction of vortical flows with  
551 poroelastic layers such as filamentous walls, the necessity of which was recently emphasized in the  
552 review of Bottaro (Bottaro 2019) for the purpose of near-wall control of turbulent boundary layer  
553 flows using engineered poroelastic coatings. The results for the filamentous canopies studied herein  
554 (see Tab. 1) have shown three major aspects of the vortex-impact induced resuspension:

555 • Flexibility of the posts increases the efficient resuspension by the amount it allows the  
556 indentation of the compliant interface (reducing the effective canopy-height) due to the  
557 bending of the flexible structures. Scaling of the results with the effective canopy height leads  
558 to a collapse of the curves for the observed resuspension in the history of several successive  
559 impacts when comparing the rigid with the flexible canopy. This result should be independent  
560 of the arrangement of the filaments in the canopy. It is interesting to further investigate if the  
561 observed effect can be predicted alternatively by an effective increase of the local  
562 permeability of the flexible canopy where filaments bend away from each other (the pore-size  
563 opens up locally). This can be tested assuming roughly that permeability scales with pore-size  
564 squared, exact relations can be found in (Sangani and Acrivos 1982).

565

566

567 • The pattern of resuspension of an initially homogeneous sand-layer in the canopy is  
568 determined by the local structure of the canopy. In the experiment with a hexagonal  
569 arrangement, the preferred pathways in this anisotropic (poroelastic) layer change the  
570 transport paths of the particles. Although the head-on impacting vortex is initially a symmetric  
571 structure, the observed crater pattern transforms quickly into a hexagonal shape. Stronger  
572 transport is observed along the preferential pathways where the filament bends less than in  
573 the directions of higher canopy resistance. Note that the impacting vortex ring generates a  
574 pattern of six radial jets which are aligned with the preferential pathways in the hexagonal  
575 pattern, as shown in our previous study (Li and Bruecker 2018).

576

577 • Comparing a layer with randomly arranged filaments with the hexagonal structure at the same  
578 average porosity show a dramatic decrease of the overall average resuspension efficiency. It  
579 needs roughly double amount of impacts to obtain the same amount of particle redistribution  
580 on average in the impact region. This proves that the preferential pathways in the canopy play  
581 a large role in resuspension. The random path of the particles around the filaments is affected  
582 in a non-linear manner by the local resistance. Regions of locally sparse arrangements of the  
583 filaments cannot balance the trapping effect of particles within regions of dense arrangement  
584 in their travel history. Nevertheless, flexibility helps again to improve resuspensions, similar  
585 as observed in the hexagonal arrangement.

586

587 Restrictions in the choice of material for the filaments to obtain full transparency of the canopy and  
588 the associated special manufacturing conditions have so far not enabled us to examine a larger  
589 parameter space. Nevertheless, the results point to the fact that measurements of the local effective  
590 height of the canopy layer may be useful to include into models for particle transport in canopies as  
591 the data overlap when scaled with the effective height of the canopy layer as the characteristic  
592 reference scale. In addition, statistical measurements of the effective canopy layer height in turbulent  
593 flow over flexible canopies could be helpful to find correlations to local differences in erosion  
594 processes.

595

## 596 Acknowledgment

597 Prof. Bruecker holds the BAE SYSTEMS Sir Richard Olver Chair in Aeronautical Engineering and the  
598 Royal Academy of Engineering Research Chair in Nature-inspired flow sensing and manipulation. The  
599 position is co-sponsored by BAE SYSTEMS and the Royal Academy of Engineering, which is gratefully  
600 acknowledged herein. The position of MSc Qianhui Li was supported by the German Research  
601 Foundation in the grant DFG 1494/32-1 which is also gratefully acknowledged. We thank Prof. Uwe  
602 Schnakenberg from IWE1, RWTH Aachen, Germany, for support in building the transparent canopies.

603

## 604 References

- 605 Bandyopadhyay, PR, and R Balasubramanian. 1995. "Vortex Reynolds number in turbulent boundary  
606 layers." *Theoretical and Computational Fluid Dynamics* no. 7 (2):101-117.
- 607 Bethke, Nastja, and Stuart B Dalziel. 2012. "Resuspension onset and crater erosion by a vortex ring  
608 interacting with a particle layer." *Physics of Fluids* no. 24 (6):063301.
- 609 Bottaro, Alessandro. 2019. "Flow over natural or engineered surfaces: an adjoint homogenization  
610 perspective." *Journal of Fluid Mechanics* no. 877.
- 611 Brücker, Ch. 2011. "Interaction of flexible surface hairs with near-wall turbulence." *Journal of Physics:*  
612 *Condensed Matter* no. 23 (18):184120.
- 613 Brücker, Ch, D Bauer, and H Chaves. 2007. "Dynamic response of micro-pillar sensors measuring  
614 fluctuating wall-shear-stress." *Experiments in fluids* no. 42 (5):737-749.
- 615 De Langre, Emmanuel. 2008. "Effects of wind on plants." *Annu. Rev. Fluid Mech.* no. 40:141-168.
- 616 Dewenter, Jana, Peggy Gerullis, Alexander Hecker, and Stefan Schuster. 2017. "Archerfish use their  
617 shooting technique to produce adaptive underwater jets." *Journal of Experimental Biology* no.  
618 220 (6):1019-1025.
- 619 Li, Qianhui, and Christoph H Bruecker. 2018. "Vortex interaction with a rough wall formed by a  
620 hexagonal lattice of posts." *Physics of Fluids* no. 30 (5):054107.
- 621 Munro, Richard J, N Bethke, and SB Dalziel. 2009. "Sediment resuspension and erosion by vortex  
622 rings." *Physics of Fluids* no. 21 (4):046601.
- 623 Nepf, Heidi M. 2012. "Flow and transport in regions with aquatic vegetation." *Annual review of fluid*  
624 *mechanics* no. 44:123-142.
- 625 Ouriemi, Malika, Pascale Aussillous, Marc Medale, Yannick Peysson, and Élisabeth Guazzelli. 2007.  
626 "Determination of the critical Shields number for particle erosion in laminar flow." *Physics of*  
627 *Fluids* no. 19 (6):061706.

- 628 Sangani, Ashok Shantilal, and A Acrivos. 1982. "Slow flow past periodic arrays of cylinders with  
629 application to heat transfer." *International journal of Multiphase flow* no. 8 (3):193-206.
- 630 Schmitz, GJ, Ch Brücker, and P Jacobs. 2005. "Manufacture of high-aspect-ratio micro-hair sensor  
631 arrays." *Journal of micromechanics and microengineering* no. 15 (10):1904.
- 632 Sundin, Johan, and Shervin Bagheri. 2019. "Interaction between hairy surfaces and turbulence for  
633 different surface time scales." *Journal of Fluid Mechanics* no. 861:556-584.
- 634 Sutherland, Alex J. 1967. "Proposed mechanism for sediment entrainment by turbulent flows." *Journal  
635 of Geophysical Research* no. 72 (24):6183-6194.
- 636